Journal of Catalysis 286 (2012) 224–236

Contents lists available at SciVerse ScienceDirect

Journal of Catalysis

journal homepage: www.elsevier.com/locate/jcat

Bimetallic Gold–Palladium vapour derived catalysts: The role of structural features on their catalytic activity

Claudio Evangelisti [a,*], Eleonora Schiavi [b], Laura Antonella Aronica [b], Anna Maria Caporusso [b,c], Giovanni Vitulli [c], Luca Bertinetti [d], Gianmario Martra [d], Antonella Balerna [e], Settimio Mobilio [f]

[a] CNR, Institute of Molecular Science and Technologies (ISTM), Via G. Fantoli 15/16, 20138 Milano, Italy
[b] Department of Chemistry and Industrial Chemistry, University of Pisa, Via Risorgimento 35, 56126 Pisa, Italy
[c] Advanced Catalysts S.r.l., Via Risorgimento 35, 56126 Pisa, Italy
[d] Department of Chemistry IFM & NIS Interdipartimental Centre of Excellence, Via P. Giuria 7, 10125 Torino, Italy
[e] INFN – Frascati National Laboratories, Frascati, Via E. Fermi 40, 00044 Frascati, Roma, Italy
[f] Department of Physics, University of Roma TRE, Via della Vasca Navale 84, 00146 Roma, Italy

ARTICLE INFO

Article history:
Received 29 August 2011
Revised 7 November 2011
Accepted 8 November 2011
Available online 16 December 2011

Keywords:
Au–Pd catalysts
Metal vapour synthesis
TEM and EXAFS analyses
Benzyl alcohol oxidation

ABSTRACT

A procedure to synthesize new Au–Pd bimetallic catalysts using Au and Pd vapours as reagents (metal vapour synthesis, MVS) is reported. The simultaneous co-condensation of Au and Pd vapours with acetone vapour affords Au–Pd/acetone-solvated metal atoms which have been used to deposit Au–Pd bimetallic nanoparticles on γ-alumina and titanium oxide supports. Transmission electron microscopy (TEM) analysis determined the nanoparticles dimensions (d_m = 2.2–2.4 nm) and size distribution while the X-ray absorption spectroscopy (XAS) analysis showed the presence of small bimetallic Au–Pd nanoparticles with a large amount of Au–Pd bonds. The bimetallic co-condensed systems, tested in the selective oxidation of benzyl alcohol with molecular oxygen both in toluene solvent and in solvent-free conditions, showed higher catalytic activity and selectivity than the corresponding monometallic systems as well as of the analogous systems obtained by separate evaporation of the two metals.

1. Introduction

Bimetallic systems are of great interest from both scientific and technological point of view. Their catalytic, electronic and optical properties are different from those of their pure constituent metals and are influenced by different factors: not only from particles size and shape, as in monometallic nanoparticles, but also from the atomic ratio of the metals and the electronic and chemical structure of bimetallic nanoparticles [1–3]. Among the numerous metals which were investigated in combination, gold–palladium systems have been extensively studied because of their peculiar catalytic properties [4]. Bimetallic gold–palladium catalysts have been recently reported as promoters of processes such as oxidation of alcohols to corresponding aldehydes or ketones [5–7], production of hydrogen peroxide [8,9], production of vinyl acetate [10,11], hydrogenation of unsaturated compounds [12,13] and hydrodechlorination of chloro- and chlorofluorocarbons [14].

Recently, several investigations towards the relationship between catalytic activity and structural and electronic features of Au–Pd bimetallic catalysts have been reported. Au and Pd can form solid solutions at any ratio [15] and depending on their preparation method, Au–Pd bimetallic systems can contain different structural features including core–shell structure [8,16–18], segregated Au and Pd monometallic domains [19], uniform Au–Pd alloys [20,21] or a mixture of them [22,23].

In this work, we report the preparation of supported Au–Pd bimetallic systems by using Pd and Au vapours as reagents (metal vapour synthesis, MVS) [24] following two different synthetic procedures. In the first one, Au and Pd vapours were co-condensed simultaneously with acetone vapour in order to obtain a close interaction between the two metals, leading to a bimetallic Au–Pd/acetone solvated metal atoms (SMAs) solution. Then, Au–Pd/acetone SMA was used as starting material to synthesize bimetallic [Au–Pd] catalysts supported on γ-alumina and titanium oxide, respectively. In the second one, Au and Pd were evaporated separately in two different evaporation reactions; therefore, Pd/acetone and a Au/acetone SMA were achieved. Afterwards, Pd and Au SMA were mixed together and used as starting materials to obtain supported [Au][Pd] bimetallic systems.

In order to have a further insight into the morphology and the structural properties of the Au–Pd bimetallic nanoparticles and to rationalize the role played by the two different MVS procedures used, Au–Pd bimetallic systems supported on γ-alumina and on titanium oxide were investigated by the transmission electron microscopy (TEM) and X-ray absorption spectroscopy (XAS) analyses.

* Corresponding author. Present address: CNR, Institute of Molecular Science and Technologies, Via C. Golgi 19, 20133 Milano, Italy. Fax: +39 050 2219260.
E-mail address: claudio@dcci.unipi.it (C. Evangelisti).

0021-9517/$ - see front matter © 2011 Elsevier Inc. All rights reserved.
doi:10.1016/j.jcat.2011.11.007

The catalytic activity of Au–Pd bimetallic systems was studied in the selective oxidation of benzyl alcohol to benzaldehyde, chosen as test reaction, evidencing a close relationship between the structural features of these bimetallic systems, induced by the different preparation procedures used, and their catalytic behaviour. The selective oxidations of alcohols to their respective aldehydes or ketones are a processes of great relevance from a laboratory and industrial point of view [25,26]. It is well known that both highly dispersed palladium [27] and gold [28] catalysts promote these processes using molecular oxygen as environmental friendly reagent respect to stoichiometrical reagents such as permanganate or dichromate, which are traditionally employed [29,30].

Recently, Au–Pd bimetallic catalysts have shown to be very active in these reactions evidencing a beneficial interaction between the two metals depending on the structural characteristics of these bimetallic systems. Significant advances in the field has been reported by Dimitratos et al. [31] and Enache et al. [6] which achieved high catalytic efficiency under solvent and solvent-free conditions, respectively, with supported Au–Pd bimetallic nanoparticles obtained by reduction in Au and Pd salts.

2. Experimental

2.1. General

All operations involving the MVS products were performed under a dry argon atmosphere. The co-condensation of gold, palladium and acetone vapours was carried out in a static reactor similar to those previously described [32]. In the case of co-evaporation experiments, the MVS apparatus was equipped with two alumina-coated tungsten crucibles heated by Joule effect with two Rial AEJ2 generators, respectively, with a maximum power of 2 kW that allowed to evaporate independently two metals. The acetone-solvated metal atoms solutions were handled under argon atmosphere with the use of the standard Schlenk techniques. The amount of palladium and gold in the above solutions was determined by inductively coupled plasma–optical emission spectrometers (ICP–OES) with a Spectro-Genesis instrument equipped with a software Smart Analyser Vision. For ICP–OES, a sample (1 mL) of SMA solutions was heated over a heating plate in a porcelain crucible in the presence of *aqua regia* (2 mL) for four times, dissolving the solid residue in 0.5 M aqueous HCl. The limit of detection (lod) calculated for palladium and gold was 2 ppb. Acetone was purified by conventional methods, distilled and stored under argon. Commercial γ-Al_2O_3 (Chimet product, type 49, 3.1 μm average particle size, surface area 110 $m^2\,g^{-1}$), TiO_2 (Degussa product, powder containing anatase (80 wt.%) and rutile (20 wt.%), P99.5%, 21 nm average particle size, surface area 50 ± 15 $m^2\,g^{-1}$) were dried in a static oven before use. Benzyl alcohol was supplied from Aldrich and used as received. The GLC analyses were performed on a Perkin–Elmer Auto System gas chromatograph, equipped with a flame ionization detector (FID), using a SiO_2 column (BP-1, 12 m × 0.3 mm, 0.25 μm) and helium as carrier gas.

Electron micrographs were obtained by a Jeol 3010-UHR high-resolution transmission electron microscope (HRTEM) equipped with a LaB_6 filament operating at 300 kV) equipped with an Oxford Inca Energy TEM 300 EDS X-rays analyser. Before the introduction in the instrument, the samples, in the form of powders, were ultrasonically dispersed in isopropyl alcohol and a drop of the suspension was deposited on a copper grid covered with a lacey carbon film. Histograms of the particle size distribution were obtained by counting onto the micrographs at least 300 particles; the mean particle diameter (d_m) was calculated by using the formula $d_m = \Sigma d_i n_i / \Sigma n_i$ where n_i was the number of particles of diameter d_i. TEM analysis was performed on both monometallic and bimetallic samples supported on Al_2O_3 and TiO_2. The instrument condition at the time of the measurements resulted in a minimum cross section of the electron beam during EDX analysis of ca. 5 nm.

The X-ray absorption spectroscopy (XAS) measurements at the Au L_3 edge (11,919 eV) and at the Pd K-edge (24,350 eV) were performed at the GILDA beamline [33] of the European Synchrotron Radiation Facility (ESRF, Grenoble). The X-ray beam was monochromatized and horizontally focused by using a double crystal Si(3 1 1) monochromator [34]; two Pd mirrors at the Au L_3 edge and two Pt mirrors at the Pd K-edge were used to reject the higher harmonics and focus the beam in the vertical direction [33]. XAS measurements at the Au L_3 and at the Pd K edges were performed on the two reference samples (Au and Pd foils) and on a complete set of two monometallic (Au (1%) and Pd (0.5%) and two bimetallic [Au][Pd], [AuPd] samples supported on γ-Al_2O_3. Two bimetallic [Au][Pd], [AuPd] samples supported on TiO_2 were measured only at the Au L_3 edge. The catalytic samples were prepared for the X-ray absorption spectroscopy (XAS) experiments mixing their fine powders with boron-nitride and pressing them into pellets. The different sample amounts were calculated [35] in order to achieve appropriate edge jumps.

Both reference samples and the catalysts at the Au L_3 edge were measured in transmission mode with two Ar-filled ionization chambers to detect the incident (I_0) and transmitted (I_T) X-ray beam. The catalysts at the Pd K-edge were measured in fluorescence mode (I_F) by using a 13-element high-purity Ge multi-detector coupled to an X-ray pulse digital analyser for a more accurate dead-time effect correction [36].

The absorption coefficients were calculated as $\mu(E) = \ln(I_0/I_T)$ in transmission mode and as $\mu(E) = (I_F/I_0)$ in fluorescence mode. All spectra were recorded at 20 K in order to reduce the thermal effects.

2.2. Preparation of the [AuPd] catalysts

In a typical experiment (Scheme 1), palladium and gold vapours generated by resistive heating of two different alumina-coated tungsten crucibles filled with ca. 150 mg of Pd powder and 300 mg of Au pellets, respectively, were co-condensed simultaneously at liquid nitrogen temperature with acetone (100 mL) in the glass reactor chamber of the MVS apparatus for a chosen time. The reactor chamber was warmed to the melting point of the solid matrix, and the resulting red–brown solution was siphoned at a low temperature into a Schlenk tube and kept in a refrigerator at −40 °C. The metal amount recovered in SMA was about the 80 wt.% of the evaporated metal. The palladium and gold content, obtained by ICP–OES analysis, were 0.5 mg/mL of Pd and 1.0 mg/mL of Au, corresponding to a Pd/Au molar ratio = 1. 70 mL of the [Au–Pd]/acetone SMA (0.33 mmols, 35 mg of Pd and 0.35 mmols, 70 mg of Au) was added to a suspension of γ-Al_2O_3 or TiO_2 (7.00 g) in acetone (30 mL). The mixture was stirred for 12 h at room temperature. Au–Pd bimetallic nanoparticles were quantitatively deposited on the supports; the colourless solution was removed, and the light-brown solid was washed with *n*-pentane and dried under reduced pressure. By this way Au–Pd bimetallic catalysts containing 1 wt.% of Au and 0.5 wt.% of Pd, represented as [AuPd]/γ-Al_2O_3 and [AuPd]/TiO_2, respectively, were obtained.

2.3. Preparation of the [Au][Pd] catalysts

In a typical experiment (Scheme 2), palladium vapour generated by resistive heating of an alumina-coated tungsten crucible filled with ca. 200 mg of Pd powder was co-condensed at liquid nitrogen temperature with acetone (100 mL) in the glass reactor chamber of the MVS apparatus for a chosen time. The reactor

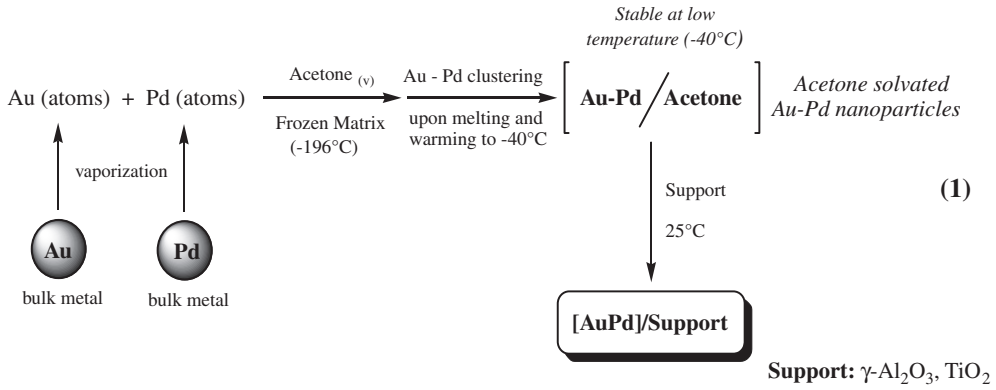

Scheme 1.

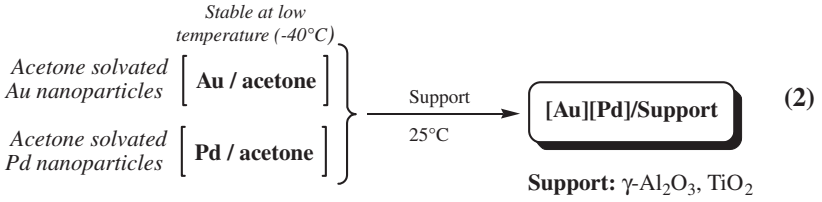

Scheme 2.

chamber was warmed to the melting point of the solid matrix, and the resulting brown solution was siphoned at a low temperature into a Schlenk tube and kept in a refrigerator at −40 °C. The palladium content of the Pd/acetone was 0.81 mg/mL. Similarly, 200 mg of Au pellets were co-condensed at liquid nitrogen temperature with acetone (100 mL), obtaining a red–purple solution containing 0.83 mg/mL of Au. Then, the 25 mL of Pd/acetone SMA (0.19 mmols, 20.2 mg of Pd) was added at low temperature (−30 °C) to Au/acetone SMA (49 mL, 0.2 mmols, 40.6 mg of Au). The resulting solution, represented as [Au][Pd]/acetone SMA containing the a Au:Pd molar ratio = 1, was added to a suspension of γ-Al_2O_3 or TiO_2 (4.06 g) in acetone (20 mL). The mixture was stirred for 12 h at room temperature. The colourless solution was removed and the light-brown solid was washed with *n*-pentane and dried under reduced pressure. Similarly to those previously reported, these systems contained 1 wt.% of Au and 0.5 wt.% of Pd.

2.4. Catalytic oxidation of benzyl alcohol in toluene

In a typical experience, in two-necked round-bottom flask (100 mL) equipped with a stirring magnetic bar, a silicon stopper and a glass cannula, connected to the oxygen reservoir, catalyst (60 mg), toluene (10 mL) and benzyl alcohol (0.31 mL, 3.0 mmol) were added. The reaction mixture was kept at 0.1 MPa of O_2, at 60 °C and the stirrer was set at 1250 rpm. The progress and the composition of the reaction mixture were determined by GLC analysis of liquid samples taken from the stoppered side neck with a syringe.

2.5. Catalytic oxidation of benzyl alcohol in solvent-free conditions

The oxidation experiments were performed at 0.5 MPa starting molecular oxygen pressure using a 25 mL stainless-steel autoclave equipped with a Teflon removable cylinder Jacker, a magnetic bar, a stainless-steel tap and a manometer (0.25 MPa end scale). The reactions were performed by heating the autoclave in an oil bath at 100 °C (±1 °C). In a typical experiment, the autoclave was charged with catalyst (125 mg) and benzyl alcohol (10 mL, 0.971 mol). The autoclave was then purged three times with molecular oxygen leaving the mixture at the desired oxygen pressure. The reaction was stirred (1200 rpm) at 100 °C. The reaction was monitored by GLC analysis of liquid samples removed by the tap. In the case of recycling experiments, after 8 h, the solid catalyst was separated from the mixture by filtration (0.4 μm Teflon filter) and the solution was analysed by ICP–OES to reveal the Pd and Au amount. Where indicated, the recovered catalyst was washed with acetone and re-used in further batch runs.

3. Results and discussion

3.1. TEM results

The analysis of the size distribution and dispersion of the metallic particles was performed using transmission electron microscopy (TEM). The data related to the observations carried out on the monometallic catalysts supported on γ-Al_2O_3 are reported in Fig. 1.

Concerning the Pd/γ-Al_2O_3 catalyst, for the most part of the sample regions inspected, EDX analysis revealed the presence of Pd, but no metal particles large enough in size ($\geqslant$1.0 nm) to be detected by TEM were observed (Fig. 1A), indicating a very high dispersion of the metal phase. Only in few regions, some Pd particles with sizes in the (1.5–5.5) nm range were found (their number was too low to obtain a statistically significant size distribution) so they represent a very minor fraction of the supported particles (Fig. 1A). Conversely, a number of metal particles quite homogeneously distributed on the alumina grains appeared in the images of Au/γ-Al_2O_3, exhibiting a kind of bimodal size distribution, with the 97% of gold particles having a size distribution between 1.5 and 7.0 nm (d_m = 4.5 ± 0.2 nm), and the rest between 7.5 and 10.0 nm (Fig. 1B), in agreement with the results reported in Ref. [46].

Moving to the bimetallic catalysts supported on alumina (Fig. 2), for both [AuPd]/γ-Al_2O_3 (section A) and [Au][Pd]/γ-Al_2O_3 (section B) samples, the support appeared densely populated by nanometric metal particles. As indicated by the size distributions,

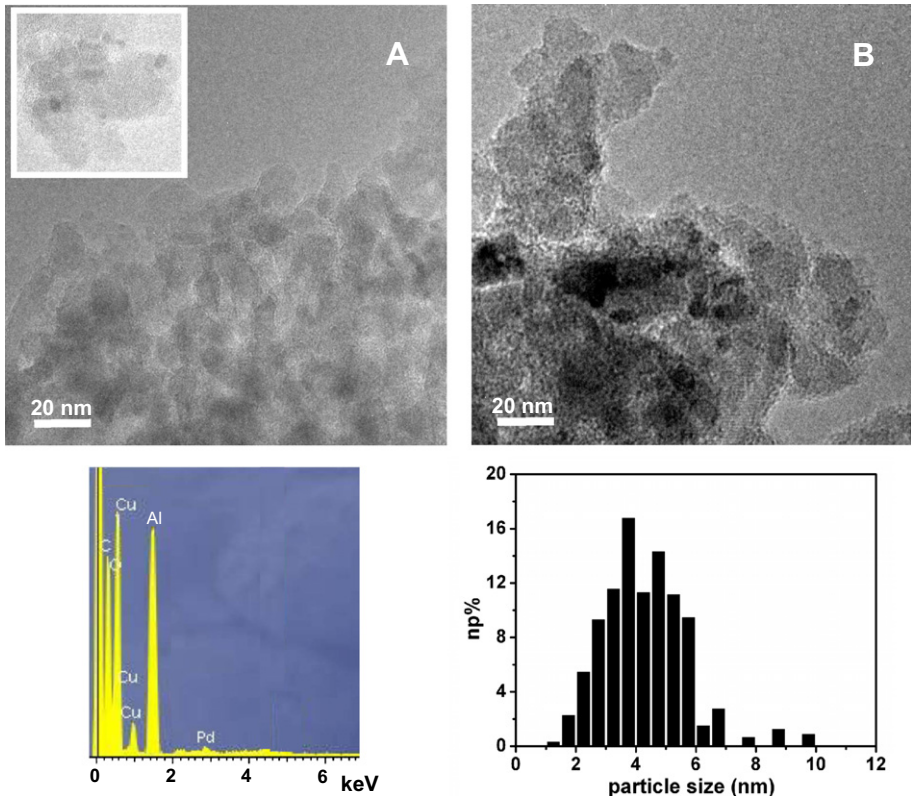

Fig. 1. TEM/EDX data obtained for Pd/γ-Al_2O_3 (section A) and Au/γ-Al_2O_3 (section B). Data in section A: main frame, image representative of the overwhelming part of the Pd/γ-Al_2O_3 catalyst; inset: image representative of the few zones with metal particle observable by TEM; lover panel: EDX spectrum of the region displayed in the main frame (Cu signals are due to the sample holder). Data in section B: image representative of Au/γ-Al_2O_3 and histogram of the metal particle size distribution obtained for this catalyst.

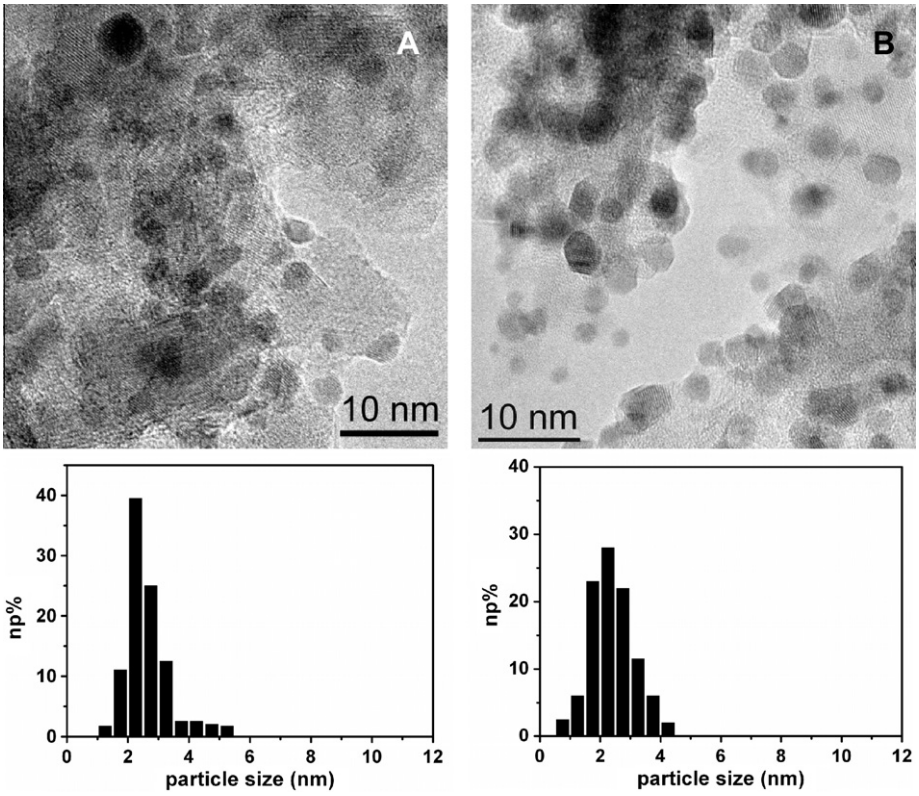

Fig. 2. TEM micrographs and metal particle size distributions of [Au][Pd]/γ-Al_2O_3 and [AuPd]/γ-Al_2O_3 (sections A and B, respectively).

their sizes lie in a quite narrow range (1–6 nm), but while in the [AuPd] case, the nanoparticles are homogeneously and symmetrically distributed around a mean size of about 2.4 ± 0.1 nm, and in the [Au][Pd] case, the distribution is quite different. In the [Au][Pd] sample about the 70% of the nanoparticles exhibits a size distribution between 2 nm and 3 nm and a d_m of 2.6 ± 0.1 nm but there is also a minor population of larger particles with sizes between 4 nm and 5.5 nm (about 10% in number, corresponding to about 40% in volume), indicating the presence of at least two families of nanoparticles. The presence of pure Au in these largest particles, consistently with that observed in the monometallic Au/γ-Al_2O_3 sample, could not be excluded.

Noticeably, the limits and the mean values of the size distributions found for the bimetallic samples are shifted towards values smaller than the ones found for Au/γ-Al_2O_3, while they are definitely larger than in the Pd/Al_2O_3 case, where most of the metallic phase was too small in size to be detected by TEM. It can be surely inferred that in both bimetallic catalysts preparation procedures, nucleation and growth of supported particles are affected by the co-presence of the two metals. As for the localization of the two metals, EDX analysis indicated that both Pd and Au were present in the regions exhibiting supported particles. Unfortunately, the particles appeared too close to each other to prevent separated analysis. Thus, the possibility to obtain information on the nature of metal particles by their structural features was attempted, by analysing images taken in high magnification–high resolution (HR) conditions (Fig. 3).

For both catalysts, supported particles exhibited interference fringes between 0.223 and 0.237 nm. The fringes are extended over the whole particles, indicating the single nanocrystals nature of the supported metals, and the spacing values are compatibles with d_{111} of the two metals that is 0.235 nm vs. 0.224 nm for Au and Pd, respectively. Unfortunately, the difference in the d_{111} of the Au and Pd was too small to allow a distinction by HRTEM between the two metals or between a metal and a possible bimetallic alloy (the highest possible resolution we could achieve was 0.012 nm/pixel, resulting in the possibility to determine lattice spacings with a precision of about 5%).

It is of interest to notice that [AuPd] particles are mostly isolated and only rarely they touch each other, eventually giving rise to limited contact interfaces, while in the [Au][Pd] case, agglomerates of 3–10 particles can be observed much more frequently, resulting in more extended contact interfaces.

As for the catalysts supported on TiO_2, the monometallic ones exhibited an high metal phase dispersion because no particles were observed neither for Pd/TiO_2 (Fig. 4A) nor for Au/TiO_2 (Fig. 4B) but the EDX signals of the metals were detected. These results are similar to ones achieved in the Pd/γ-Al_2O_3 case, whereas the difference with respect to the Au/γ-Al_2O_3 ones shows a significant role of the support in the formation of gold nanoparticles. Previously reported studies on Au particle size growth in solution [37] showed as the differences in metal particle sizes, evidenced by TEM analyses, can be related to the different deposition time of metal particles on the support.

The metal dispersion appeared to be quite high also in the case of [Au][Pd]/TiO_2 (Fig. 5A), where most of the titania particles seemed to be 'naked' in TEM images, but not in the EDX spectra, and only in some cases, few metal particles with size ranging from 1.0 to 7.0 nm were observed (Fig. 5A), clearly not enough to obtain a statistically significant size distribution.

Differently, supported particles appeared more abundant in the [AuPd]/TiO_2 sample (Fig. 5B), although less densely distributed on the support than in the [AuPd]/γ-Al_2O_3 case. By considering that the specific surface area of the titania powder used is about one half of that of alumina, if the [AuPd]/TiO_2 supported particles observed in TEM images should correspond to the total amount of metals present on the support, a much higher particle density should be present. In this respect, it could be considered that although the mass density of TiO_2 and alumina can be similar, that latter is often constituted by thin particles, in the form of 'platelets' [38], resulting more transparent to the electron beam than TiO_2 particles.

Thus, on the basis of the higher dispersion of the monometallic catalysts, and on the asymmetry of the size distribution of particles observed by TEM on [AuPd]/TiO_2, it can be proposed that a significant number of metal particles too small to be detected by TEM may be present, likely representing the majority of the supported phase. As for the nature of the observed particles, they were not still separated enough to obtain unambiguous EDX results, and the analysis of structural data suffered of the limitation reported above.

3.2. XAS results

The XAS measurements of the Au and Pd foils were used to calibrate the energy scales, to align the XAS spectra and to evaluate and fix the respective S_0^2 values.

The extended X-ray absorption fine structure spectra (EXAFS), usually indicated as $\chi(k)$, are given by the normalized oscillations superimposed onto the measured absorption coefficient $\mu(k)$. Quantitatively they are defined as follows:

$$\chi(k) = [(\mu(k) - \mu_0(k)]/\mu_0(k)$$

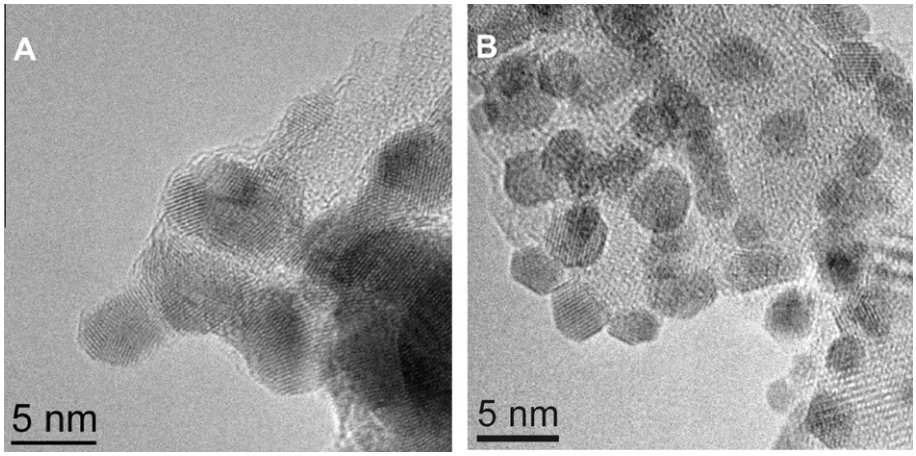

Fig. 3. HR-TEM micrographs: interference fringes observed for [Au][Pd] γ-Al_2O_3 and [AuPd]//γ-Al_2O_3 (sections A and B, respectively).

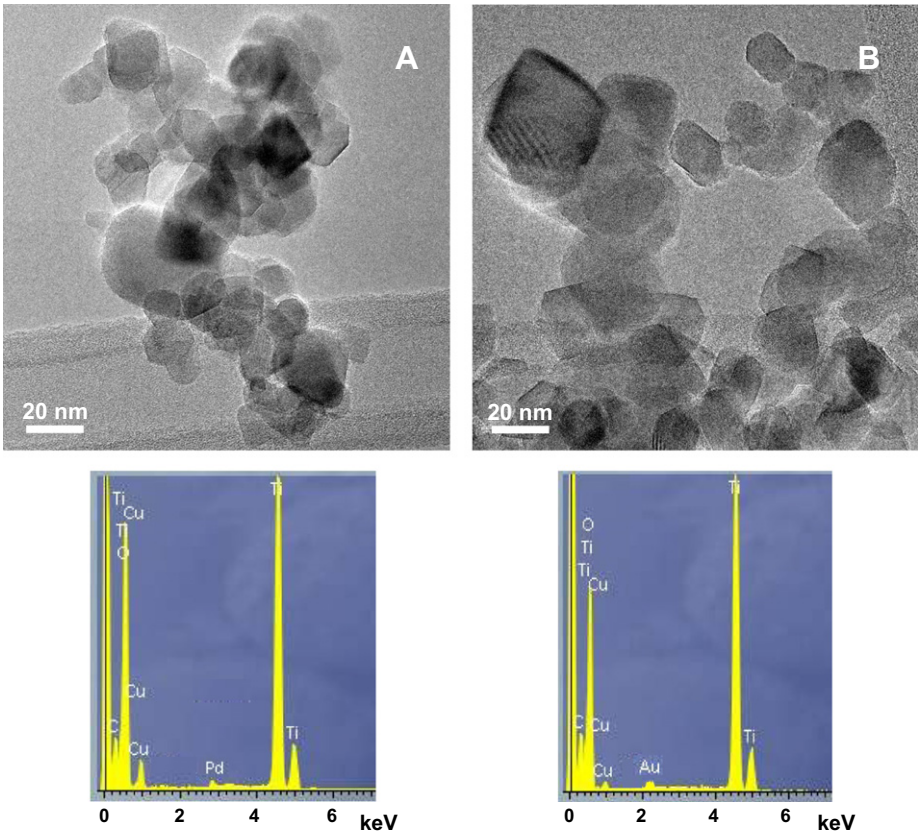

Fig. 4. TEM/EDX data obtained for Pd/TiO_2 (section A) and Au/TiO_2 (section B). Cu signals in EDX spectra are due to the sample holder.

where $\mu_0(k)$ is the total atomic absorption coefficient and k is the photoelectron wave vector; it is given by

$$k = [4\pi m(E - E_0)/h^2]^{1/2}$$

where E is the incoming photon energy and E_0 is the threshold energy; as usually it was determined as the inflection point of the measured absorption edge.

The EXAFS spectra were extracted from the experimental X-ray absorption spectra according to standard procedures [39]; they are reported in Fig. 6 and in the upper panel of Figure for Au L_3 and Pd K edges, respectively. In Fig. 7 and in the lower panel of Fig. 8, their Fourier Transforms (FT) are reported. FT are composed of a series of peaks: the first peak centred at about 2.75 Å for Au and at about 2.5 Å for Pd corresponds to the first 12 neighbours of the fcc structures and the other peaks correspond to the outer coordination shells. While the first peak comes only from single scattering contributions, the others are due to the superposition of single and multiple scattering contributions. To perform an accurate data analysis [40], we took into account all these multiple scattering contributions [40]; data were best fitted to simulated spectra built using theoretical amplitudes and phases provided by the FEFF8 code [41,42]. Data fitting was performed in both R-space and k-space with k^2 (Pd) and k^3 (Au) weights; also an estimation of the accuracy of the obtained structural parameters, compatible with the data quality and k range used [43], was achieved.

In Fig. 9, the first peak in the Fourier Transform of the Au foil matches the 12 first neighbours at an effective distance of about 2.88 Å in the bulk. The small peak at its left is due the shape of the Au back-scattering amplitude and on the used FT range and k weighting factor.

In Fig. 7, significant differences are clearly visible between the [Au][Pd] and the [AuPd] samples, showing that their structures are quite different.

In Fig. 8 (lower panel), the Fourier transforms of the Pd K-edge EXAFS spectra are shown; also in this case, the first peak of the Pd foil matches the 12 first neighbours that are at an effective distance of about 2.75 Å in this case. In the Fourier transforms of the samples supported on γ-Al_2O_3, the presence of a peak between 1 Å and 2 Å is clearly visible: in this case, it is due to a Pd–O contribution. Relevant differences are clearly visible between the bimetallic samples also in the FT spectra at the Pd K-edge.

In the fitting procedures of the Au bulk and Au/γ-Al_2O_3 (1 wt.%) spectra, we included single scattering (SS) e multiple scattering (MS) contributions, up to the fourth coordination shell. In the case of Pd bulk and of the monometallic Pd/γ-Al_2O_3 (0.5 wt.%), we considered contributions up to the second Pd–Pd shell. Finally, for the bimetallic samples only the first coordination shell was studied. In all the spectra of the catalysts at the Pd K-edge also the peak due to the Pd–O contribution was fitted.

To reduce the number of free parameters in the fitting of the Au bulk and Au/γ-Al_2O_3, the bond lengths of the higher order coordination shells were all linked to that of the second one according to a fcc structure, and the MS path lengths were assumed equal to the corresponding SS path lengths. In the case of Au bulk also the coordination numbers were fixed to the values of the fcc structure. The fitting curves obtained for Au bulk and the monometallic catalyst supported on Al_2O_3 are compared with the experimental spectra in the values of coordination numbers (N), nearest-neighbours distances (R) and Debye–Waller factors (σ^2) obtained are reported in Table 1. We underline the excellent agreement achieved and that the values found for the reference Au bulk sample are in good agreement with those expected and also with those found

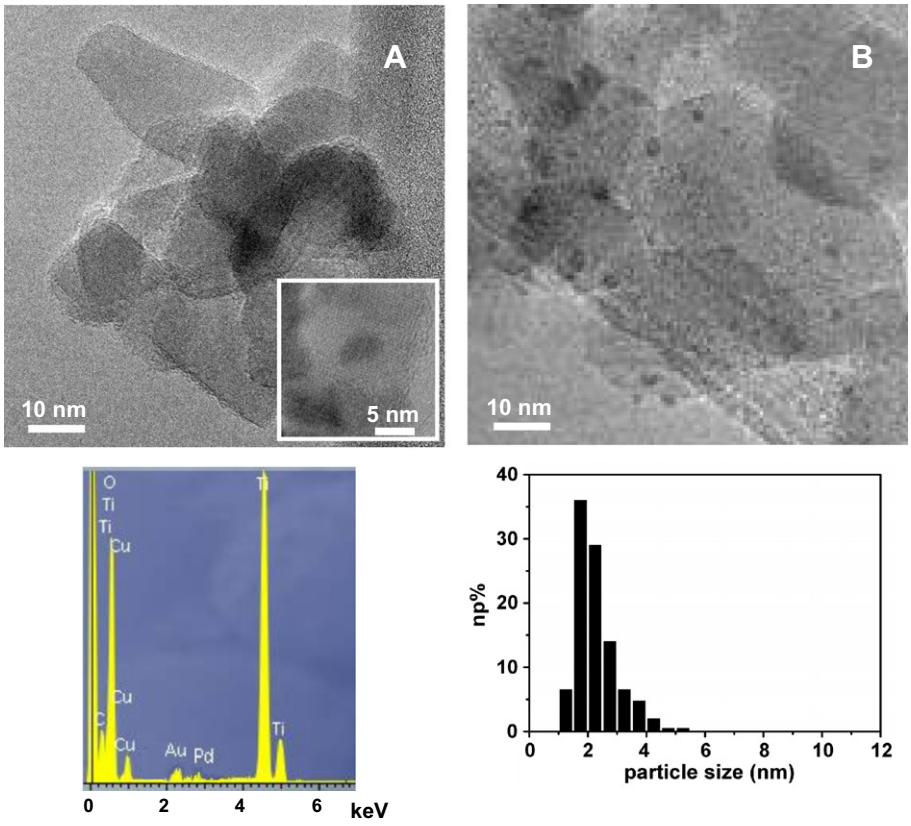

Fig. 5. TEM/EDX data obtained for [Au][Pd]/TiO_2 (section A) and [AuPd]/TiO_2 (section B). Data in section A: main frame, image representative of the overwhelming part of the [Au][Pd]/TiO_2 catalyst; inset: image representative of the few zones with metal particle observable by TEM; lover panel: EDX spectrum of the region displayed in the main frame (Cu signals are due to the sample holder). Data in section B: image representative of [AuPd]/TiO_2 and histogram of the metal particle size distribution obtained for this catalyst.

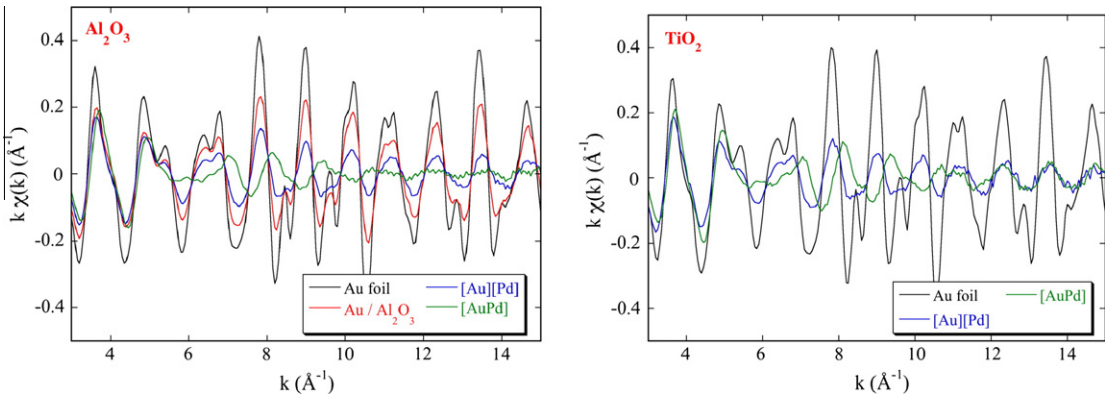

Fig. 6. Au L_3 edge EXAFS spectra of samples supported on Al_2O_3 (right panel) and on TiO_2 (left panel).

in a very detailed study [44] performed on gold bulk thermal effects.

The spectra and the values found, for all samples supported on Al_2O_3, at the Au L_3 edge and at the Pd K-edge, are reported in Fig. 10, Tables 1 and 3; the ones related to the samples supported on TiO_2 are reported in Fig. 11 and Table 2. The results achieved show interesting correlations and indicate a different environment for Au and Pd. In all samples, the first shell coordination number is lower than 12, the value of a bulk fcc metal, showing the presence of relatively small nanoparticles.

In the monometallic Au/γ-Al_2O_3 case, the reduction in the coordination numbers, *N*, can be used to estimate the average nano-particle size (*D*) [45]: assuming spherical nanoparticles, we get a diameter $D = 4.6$ nm, in agreement with the present and previously reported TEM results [46]. Also the reduction in the interatomic distance and the increase in the Debye Waller factor are compatible with the values reported for Au nanoparticles of such size [39,47].

The case of the monometallic Pd is more complicated because in this case Pd atoms are bound not only to other Pd atoms to form small nanoparticles as suggested by the reduced Pd–Pd first shell coordination number but also to oxygen atoms. This indicates a partial oxidation of the Pd clusters and/or some interaction with the oxygen atoms of the support. The presence of Pd–O and

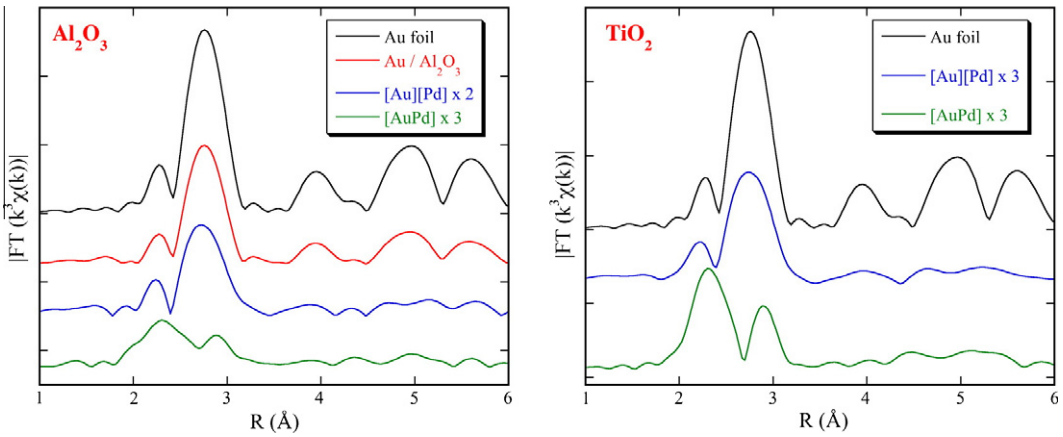

Fig. 7. Au L_3 edge k^3 weighted Fourier transforms in the k range 3.5–14 Å^{-1}.

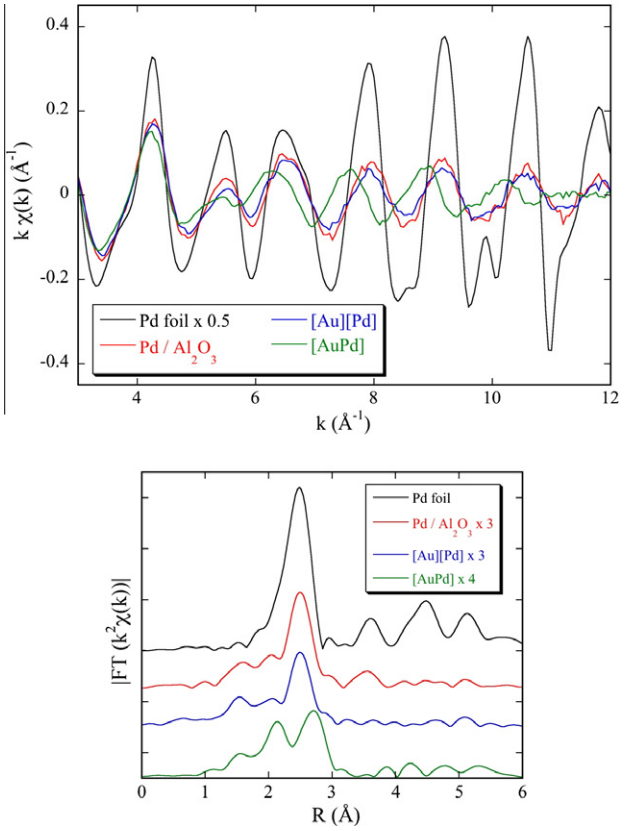

Fig. 8. Pd K-edge EXAFS spectra and corresponding k^2 weighted Fourier transforms in the k range 3–12 Å^{-1}.

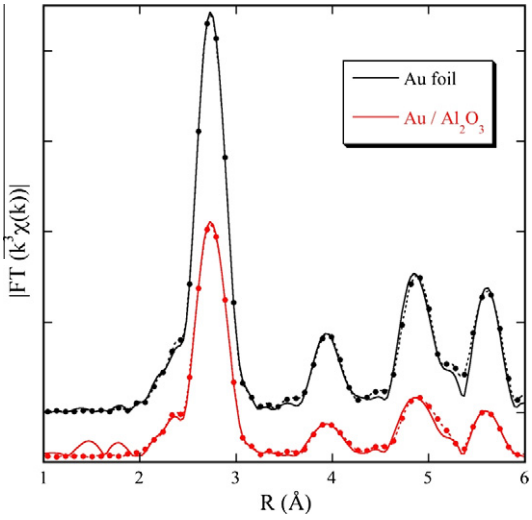

Fig. 9. Amplitudes of the Fourier transforms of the experimental signals at 20 K and the best fitting simulated signals (dotted lines).

Table 1
Distances (R), coordination numbers (N), distances and Debye Waller factors (σ^2) achieved for the Au bulk sample, for the Au monometallic catalyst and for the bimetallic samples on γ-Al_2O_3 at the Au L_3 edge.

Sample	Shell number	N	R (Å)	σ^2 (Å^2)
Au bulk	1	12(fixed)	2.875(5)	0.0020(5)
R-factor = 0.002	2	6(fixed)	4.067(7)	0.0026(7)
	3	24(fixed)	4.986(7)	0.0031(7)
	4	12(fixed)	5.758(7)	0.0032(7)
Au/γ-Al_2O_3	1	10.9(4)	2.867(5)	0.0031(8)
Au (1%)	2	5.1(2)	4.061(7)	0.0043(9)
R-factor = 0.006	3	20.3(8)	4.976(7)	0.0046(9)
	4	10.5(4)	5.749(7)	0.0050(9)
[Au][Pd]	Au–Au	10.2(9)	2.854(7)	0.0062(9)
R-factor = 0.006	Au–Pd	0.9(2)	2.793(7)	0.0063(9)
[AuPd]	Au–Au	5.5(5)	2.815(8)	0.0087(9)
R-factor = 0.005	Au–Pd	3.6(5)	2.794(8)	0.0071(9)

Pd–Pd coordinations prevents us from evaluating the Pd cluster dimensions using the Pd–Pd coordination number as in the case of Au; as a matter of fact, the value found (N_{Pd-Pd} = 5.2) is not the real coordination number of the Pd atoms nanoparticles but is the product of the unknown atomic fraction of Pd atoms in this configuration with the real coordination number.

We can, however, reach a qualitative conclusion by comparing the results reported in Tables 1 and 3 and by noting in Fig. 8 (lower panel) that in this monometallic Pd sample, differently from the Au case, the higher order coordination shell signals are very small compared with the Pd foil ones: we conclude that we are in the presence of monometallic Pd nanoparticles of dimensions rather smaller than in the monometallic Au case, in agreement with TEM results (see Section 3.1). Such small nanoparticles have an fcc structure because, as given by the EXAFS data analysis, the ratio between the second shell distance and the first one R_2/R_1 is 1.40, the value expected for an fcc structure.

As clearly visible in Table 3, small and comparable amounts of oxidized Pd are present in all the catalysts supported on Al_2O_3,

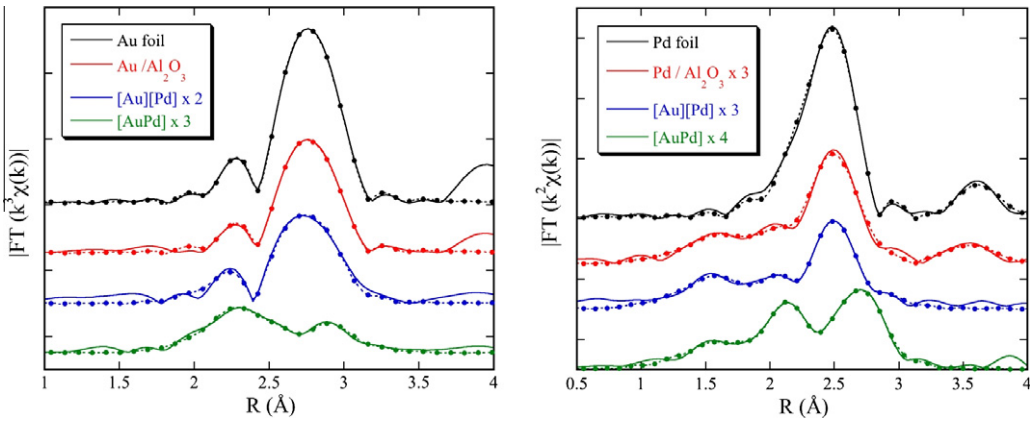

Fig. 10. Amplitudes of the Fourier transforms of the experimental EXAFS signals at 20 K and the best fitting simulated signals (dotted lines) achieved at the Au L_3 edge and at the Pd–K-edge (left panel and right panel, respectively) for the samples supported on Al_2O_3.

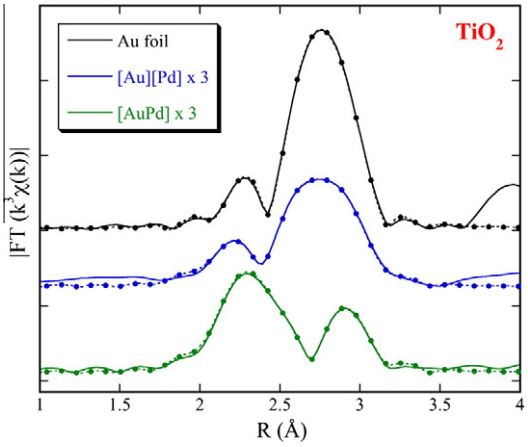

Fig. 11. Amplitudes of the Fourier transforms of the experimental EXAFS signals at 20 K and the best fitting simulated signals (dotted lines) achieved at the Au L_3 edge for the samples supported on TiO_2.

Table 2
Results achieved on the bimetallic samples on TiO_2 at the Au L_3 edge.

Sample	Shell	*N*	*R* (Å)	σ^2 (Å^2)
[Au][Pd]	Au–Au	9.5(9)	2.850(7)	0.0068(9)
R-factor = 0.006	Au–Pd	0.9(2)	2.794(7)	0.0075(9)
[AuPd]	Au–Au	5.0(5)	2.814(8)	0.0045(9)
R-factor = 0.003	Au–Pd	3.4(5)	2.793(8)	0.0031(9)

Table 3
Results achieved at the Pd K-edge.

Sample	Shell number	*N*	*R* (Å)	σ^2 (Å^2)
Pd bulk	Pd–Pd	12(fixed)	2.745(7)	0.0022(6)
R-factor = 0.003	Pd–Pd	6(fixed)	3.885(7)	0.0029(6)
Pd/γ-Al_2O_3	Pd–O	0.9(2)	2.00(1)	0.002(1)
Pd (0.5%)	Pd–Pd	5.2(6)	2.74(1)	0.007(1)
R-factor = 0.012	Pd–Pd	2.5(4)	3.84(1)	0.009(1)
[Au][Pd]	Pd–O	1.1(2)	2.00(1)	0.002(1)
R-factor = 0.013	Pd–Pd	4.3(6)	2.74(1)	0.008(1)
	Pd–Au	1.2(3)	2.79(1)	0.012(1)
[AuPd]	Pd–O	0.7(2)	2.01(1)	0.003(2)
R-factor = 0.009	Pd–Pd	2.5(5)	2.80(1)	0.005(2)
	Pd–Au	3.6(5)	2.79(1)	0.006(2)

and this can probably exclude any significant effect on the quite different catalytic activities of the bimetallic [AuPd] and [Au][Pd] samples.

In the bimetallic samples, supported on γ-Al_2O_3 and TiO_2, we clearly observe (Tables 1–3) the presence of Au–Pd bonds; their contributions are quite different in [Au][Pd] samples compared to the [AuPd] ones. In the first case, the number of Pd atoms among the Au neighbours (and the number of Au atoms among the Pd neighbours) is rather small (~10% and ~20% respectively); on the other hand, in the [AuPd] case, the presence of Au–Pd bonds is much higher.

In the [Au][Pd]/γ-Al_2O_3 sample, the values of the Au–Au and Pd–Pd coordination numbers found are compatible with those found on the monometallic samples but due the co-presence of Au and Pd atoms as nearest neighbours they cannot be used, as in the pure monometallic case, to determine the effective size of the Au and Pd nanoparticles. Only a small amount of heteroatomic Au–Pd bonds is present in the [Au][Pd]/γ-Al_2O_3 sample and it can be due to the interactions between the monometallic nanoparticles. A possible explanation could be that probably the smaller Pd nanoparticles sit on the surface of the larger Au ones giving rise to some alloying only in the boundary regions. In the [Au][Pd] sample supported on TiO_2 similar results were achieved.

In the case of the [AuPd] samples, we found that the Pd–Pd coordination numbers are smaller than the Pd–Au ones while the interatomic distances are comparable one with the other. The absence of a Pd–Pd distance of 2.74 Å suggests the absence of pure Pd nanoparticles while the presence of Pd–Pd distances comparable to the Pd–Au ones suggests the presence of a well-defined Pd–Au phase. Since the Pd:Au molar ratio is equal to 1 in the presence of a homogenous PdAu alloy, the Pd–Pd and Pd–Au coordination numbers should be the same but this is not the case because the number of Pd and Au atoms around the Pd absorber is different ($N_{Pd-Pd} \neq N_{Pd-Au}$).

Let us now consider the situation around Au; in this case, the Au–Au distances of about 2.82 Å are different from the Au–Pd and the Pd–Pd ones and are contracted with respect to the Au bulk value. This, together with the value of the Au–Au coordination numbers rather higher than the Au–Pd ones, indicates the presence of small Au-rich cores. From the value of the Au–Au distances [47], we quote a dimension of about 12 Å corresponding to a nanoparticle of about 55 atoms. From all these considerations, we conclude that in our [AuPd] samples, bimetallic Au–Pd nanoparticles, composed of an Au rich core surrounded by a AuPd alloyed shell, are present.

A physical reason of such a structure could be attributed to kinetically more favourable nucleation steps of Au atoms in acetone solution during the melting of the acetone solid matrix, followed from a slower aggregation of Au and Pd atoms on preformed Au seeds but also by the high thermodynamic stability at low temperatures (<500 K) of Au–Pd bimetallic particles having a Au rich shell [16,48]. It can be related to the different stabilization properties of acetone towards Pd and Au atoms, as observed also in alumina-supported samples derived from mononuclear Pd and Au SMA, where Pd nanoparticles are smaller than those of Au.

Comparing the results reported in Tables 1 and 2, the main structural difference between the [AuPd] samples on Al_2O_3 and TiO_2 comes from their very different Debye–Waller factors (σ^2). While the Au–Au and Au–Pd coordination numbers and distances are quite similar between their Debye–Waller factors, there is a factor 2. This difference can probably be related to the different fractions of metallic phase and size distributions found by the TEM analysis (see Section 3.1).

The different structural results achieved by the EXAFS data analysis for the [AuPd] and [Au][Pd] samples can be also qualitatively observed in the normalized experimental X-ray Absorption Near Edge Structure (XANES) spectra reported in Figs. 12.

It is well known that the Au L_3 edge probes electronic transitions from 2p to 5d states.

In Fig. 12a, the peak A is known as white line and its intensity is related to the presence of unoccupied 5d states (d-holes) [49]. In gold bulk, its presence is due to the s–p–d atomic level hybridization, which results in a partial depletion of the atomic filled $5d^{10}$ orbitals. In the nanoparticles, the reduced number of Au–Au bonds reduces the hybridization as well resulting in an increase in the 5d level occupancy and hence in a decrease in the intensity of the feature A; this is visible in Fig. 12a comparing the bulk spectrum with the [Au] monoatomic cluster case. As shown by Liu et al. [49] in Au–Pd clusters, a further reduction in the intensity of the white line (feature A) can be due to a charge transfer from Pd to Au. Therefore, the strong electronic effect observed in Fig. 12a comparing the [Au][Pd] sample to the [AuPd] one can be related to the increased Au–Pd coordination, which causes a further filling of the Au d band. These two effects observed by looking at the Au L_3 edge XANES spectra when moving from Au bulk to the [AuPd] sample that is the decrease in the intensity of white line when moving from the bulk to the Au nanoparticles and a further decrease when moving to the [AuPd] nanoparticles are the electronic counterpart of what we have found in the EXAFS spectra.

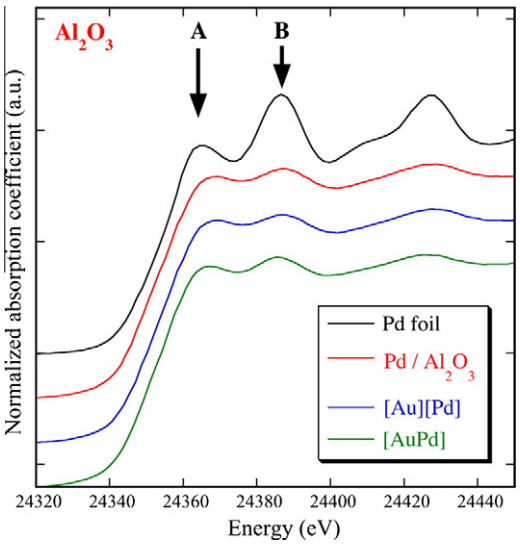

Fig. 12b. XANES spectra at the Pd K-edge of the Pd foil and of the catalysts supported on Al_2O_3.

The interpretation of the Pd XANES spectra (Fig. 12b) is complicated by the presence of oxygen. Taking into account the two features A and B present above the edge jump, it is clearly visible a reduction in their relative intensities in moving from the Pd foil to the nanostructured samples. These changes are surely related to the nanoparticles reduced dimensions and oxidation that produces electronic and structural effects [50]. The small shifts to higher energies of these XANES features observed in the Pd/γ-Al_2O_3 and [Au][Pd] spectra result from lattice contraction. The opposite shift observed in the [AuPd] sample is associated with the large amount of Au present around Pd in this sample, which, as seen by EXAFS data analysis, results in an increase in the coordination distances. Such trends are in agreement with Ref. [17] where the experimental spectra of a Pd and an Au–Pd foil are reported.

3.3. Catalytic behaviour in selective oxidation of benzyl alcohol

The Au–Pd bimetallic systems obtained by above-described two different procedures, and supported on γ-alumina and titanium oxide, were tested in the selective oxidation of benzyl alcohol to

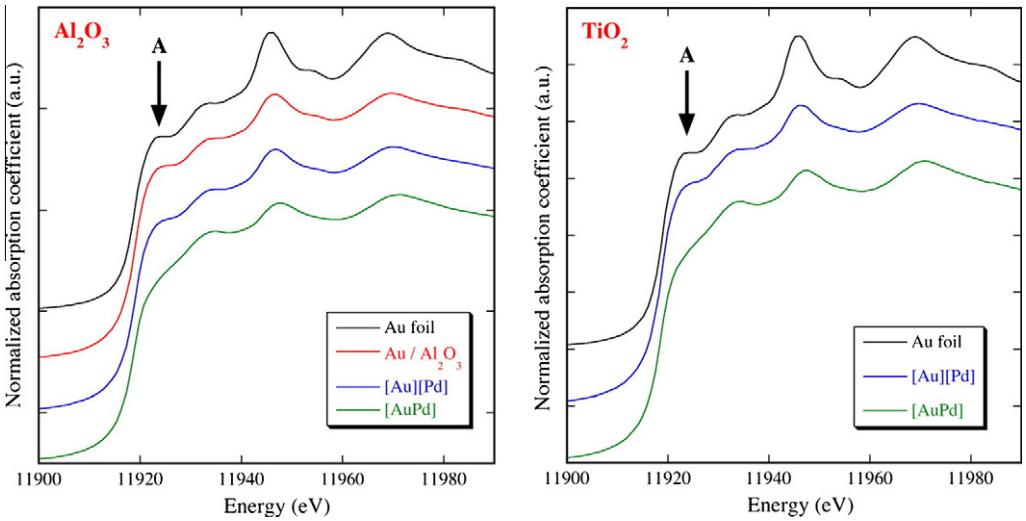

Fig. 12a. XANES spectra at the Au L_3 edge of the Au foil and of the catalysts supported on Al_2O_3 (left panel); XANES of the Au foil and of the catalysts supported on TiO_2 (right panel).

Table 4
Selective catalytic oxidation of benzyl alcohol over MVS-derived supported Au, Pd and Au–Pd bimetallic catalysts.

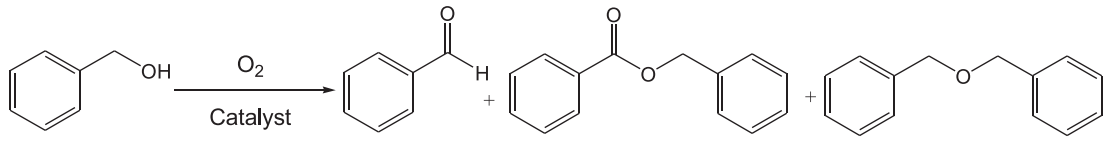

1 2 3 4

Run	Catalyst	Solvent	Time (h)	Conversion (%)	Selectivity (%)			Specific activity[b] ($\times 10^{-3}$ s^{-1})
					2	3	4	
1	Pd/γ-Al_2O_3 0.5 wt.%	Toluene	3	4.5	14	86	–	2.1
2	Au/γ-Al_2O_3 1 wt.%	Toluene	3	2.5	46	45	9	1.2
3	[Au][Pd]/γ-Al_2O_3 1 wt.% Au–0.5 wt.% Pd	Toluene	3	12	81	19	–	5.5
4	[AuPd]/γ-Al_2O_3	Toluene	3	57	84	14	2	26.4
	1 wt.% Au–0.5 wt.% Pd		6	98	91	8	1	22.7
5	Pd/TiO_2 0.5 wt.%	Toluene	3	10	53	45	2	4.7
6	Au/TiO_2 1 wt.%	Toluene	3	6	45	55	–	2.8
7	[Au][Pd]/TiO_2 1 wt.% Au–0.5 wt.% Pd	Toluene	3	11	72	28	–	5.8
8	[AuPd]/TiO_2	Toluene	3	31	90	8	2	14.4
	1 wt.% Au–0.5 wt.% Pd		12	87	93	6	1	10
9	Pd/γ-Al_2O_3 0.5 wt.%	–	2	3	44	51	5	62.5
10	Au/γ-Al_2O_3 1 wt.%	–	2	2	41	48	11	38.5
11[a]	[AuPd]/γ-Al_2O_3	–	2	25	74	14	12	250.6[c]
	1 wt.% Au–0.5 wt.% Pd		8	75	93	5	2	
12	Pd/TiO_2 0.5 wt.%	–	2	5	57	38	5	104.2
13	Au/TiO_2 1 wt.%	–	2	4	46	45	9	77.1
14[a]	[AuPd]/TiO_2	–	2	22	86	13	1	220.3[c]
	1 wt.% Au–0.5 wt.% Pd		8	73	96	4	–	

Reaction conditions: solvent = 10 ml, benzyl alcohol = 0.3 M, substrate /metal molar ratio = 500, T = 60 °C, $P(O_2)$ = 1 atm.
[a] Reaction conditions: benzyl alcohol 10 ml (0.088 mol), catalyst 125 mg, T = 100 °C, $P(O_2)$ = 5 atm.
[b] Mols of products/[(mols of Au + mols of Pd) × hour].
[c] Calculated at t = 2 h.

benzaldehyde as model reaction and their catalytic properties were compared with those of the corresponding monometallic systems. Catalytic tests were carried out in mild conditions (60–100 °C and 0.1–0.5 MPa of molecular oxygen) in both organic solvent (toluene) and solvent-free conditions as reported in Table 4. The presence of benzyl benzoate and benzyl ether was observed as by-products, whereas benzoic acid was absent.

Considering the catalytic tests in toluene solution (runs 1–8), bimetallic [AuPd] systems deriving from the simultaneous co-condensation of Au and Pd vapours and then supported on γ-Al_2O_3 and TiO_2 (see Scheme 1) (run 4 and 8, respectively) showed remarkable higher catalytic activity (SA = 26.4 × 10^{-3} s^{-1}, run 4, and SA = 14.4 × 10^{-3} s^{-1}, run 8, respectively) than the corresponding monometallic Au and Pd systems (runs 1, 2 and runs 5, 6, respectively). It is worthy to note that, among the monometallic samples, Au and Pd systems supported on TiO_2 showed slightly higher catalytic activity than analogous samples deposited on γ-Al_2O_3; these different behaviours could be related to the different size distributions found by the TEM analysis (see Section 3.1).

The above-mentioned [AuPd] bimetallic catalysts were also significantly more active than bimetallic systems prepared by MVS technique following the second procedure (see Scheme 2) (SA = 5.5 × 10^{-3} s^{-1}, run 3 and SA = 5.8 × 10^{-3} s^{-1}, run 7). Moreover, [AuPd]/γ-Al_2O_3 (run 4) and [AuPd]/TiO_2 (run 8) catalysts showed the highest selectivity towards benzaldehyde (run 4, Sel. = 91% at 98% of benzyl alcohol conversion and run 8, Sel. = 93% at 87% at benzyl alcohol conversion, respectively). Similarly to that previously observed [6,17,31], the above-reported catalytic results together with XAS analyses show that the high catalytic efficiency, in terms of activity and selectivity, of Au–Pd bimetallic systems is mainly caused by electronic interaction between the components, as well as geometric effect due to changes in lattice constants induced by a direct interaction between Pd and Au atoms. As evidenced by XANES data analyses, the increased Au–Pd coordination in [AuPd] samples leads to a charge transfer from Pd to Au causing a further filling of the Au–Pd bond, on the other hand EXAFS data showed an increased coordination distances in these samples. Conversely, [Au][Pd]/γ-Al_2O_3 and [Au][Pd]/TiO_2 systems obtained from interactions of previously formed Pd and Au nanoparticles having comparable metal particle size distributions with respect to the analogous [AuPd] samples (see TEM analyses, Section 3.1) and a smaller amount of hetero-atomic Au–Pd bonds (see EXAFS analyses, Section 3.2) did not show any increase in catalytic activity, although higher selectivity, with respect to the monometallic systems.

The comparison between the catalytic results obtained with [AuPd] bimetallic catalysts on the different supports shows that, although HRTEM analyses indicated rather smaller metal particle sizes in TiO_2-supported system, the catalytic activity of [AuPd]/γ-Al_2O_3 system (run 4) was higher than that of [AuPd]/TiO_2 (run 8). However, TiO_2-supported systems showed higher selectivity than the analogous sample supported on γ-Al_2O_3. The difference in selectivity between the two catalysts appears more evident at low benzyl alcohol conversion, where [AuPd]/TiO_2 sample led to the formation of lower amount of benzyl benzoate. The mechanism by which benzyl benzoate are formed was previously described [6,51] and involves a condensation reaction between the generated aldehyde and the initial alcohol which is catalysed by the acid–basic sites present on the catalyst. These data seem to indicate that the weaker acid sites of titanium oxide-supported catalyst limit the formation of benzyl benzoate at low benzyl alcohol conversion. Moreover, it is interesting to note that in both cases the selectivity

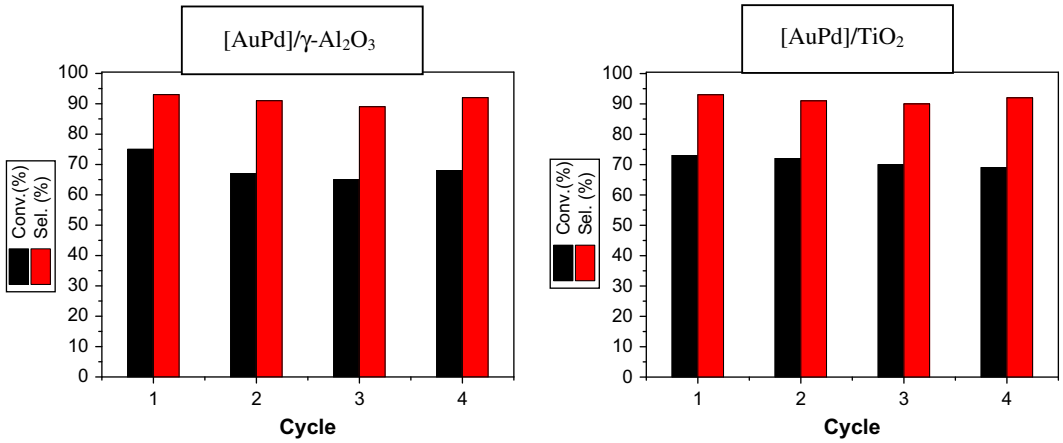

Fig. 13. Recycling tests in solvent-less batch runs of [AuPd]/γ-Al_2O_3 and [AuPd]/TiO_2 left side and right side, respectively. (Reaction conditions: benzyl alcohol 10 ml (96 mmols), catalyst 125 mg, T = 100 °C, $P(O_2)$ = 5 atm, t = 8 h).

to benzaldehyde increased at high alcohol conversion whereas a decrease in by-product formation, including benzyl benzoate, was observed.

Taking into account the high catalytic efficiency of [AuPd]/γ-Al_2O_3 and [AuPd]/TiO_2 systems, they were also tested in the same reaction under solvent-free conditions comparing their catalytic efficiency with those of the corresponding monometallic systems. Similarly to that observed for reactions performed in toluene solution, the bimetallic [AuPd] systems (run 11 and run 14, respectively) are significantly more active and selective than the corresponding monometallic ones (runs 9 and 10, and runs 12 and 13, respectively). The catalysts showed high activity (SA = 250.6×10^{-3} s^{-1} and SA = 220.3×10^{-3} s^{-1}, respectively) and high selectivity towards benzaldehyde at about 75% of alcohol conversion. Again, at low benzyl alcohol conversion, the [AuPd]/TiO_2 sample showed higher selectivity than [AuPd]/γ-Al_2O_3 which led to the formation of dibenzylether as main by-product that, similarly to the above-described benzyl benzoate formation, could be catalysed by the acid–basic sites of the catalyst [51].

Leaching tests, performed by ICP–OES analyses, on [AuPd]/γ-Al_2O_3 and [AuPd]/TiO_2 systems in solvent-free conditions, revealed gold and palladium amounts in solution lower than 0.2% of the total available metal. Accounting the very low metal leached during the reaction, recycling tests with [AuPd]/γ-Al_2O_3 and [AuPd]/TiO_2 catalysts in subsequent solvent-free batch runs were carried out. As showed in diagrams reported in Fig. 13, both catalysts were recycled for four batch runs without no significant loss in catalytic activity and selectivity.

4. Conclusions

Bimetallic Au–Pd nanostructured systems supported on Al_2O_3 and TiO_2 have been conveniently prepared using Au and Pd vapours as reagents. Two alternative routes have been adopted: (1) direct vaporization of the two metals ([AuPd]) and (2) mixing separately prepared Au and Pd precursors ([Au][Pd]).

TEM analysis has shown the high metal phase dispersion mainly present in the monometallic samples on TiO_2 and on the monometallic Pd/γ-Al_2O_3 sample. Both bimetallic [AuPd] and [Au][Pd] systems deposited on alumina show metal particles ranging 1.0–6.0 nm in diameter while the analogous systems deposited on titania present a significant number of metal particles too small to be detected by TEM (<1.0 nm) as confirmed also by XAS analysis.

XAS investigations on the bimetallic catalysts derived from routes 1 and 2 have shown quite different structural features. In the samples prepared by simultaneous vaporization of the two metals (route 1), nanoparticles composed of an Au rich core surrounded by an Au–Pd alloyed shell have been evidenced. In the samples prepared by route 2, monometallic Au and Pd nanoparticles and a small presence of hetero-atomic Au–Pd bonds were found. A possible explanation of the presence of hetero-atomic bonds could be given by the sitting of the smaller Pd nanoparticles on the surface of the larger Au ones giving rise to some alloying only in the boundary regions.

The catalytic activity of the samples obtained by routes 1 and 2, evaluated in the oxidation of benzyl alcohol with molecular oxygen, as a reference reaction, is quite different; [AuPd]/γ-Al_2O_3 and [AuPd]/TiO_2 samples obtained by route 1 resulted largely more active and selective than analogous samples prepared by route 2, pointing out the relevance of the different structural features of catalysts prepared in different ways in such reaction. These results are in agreement with previously reported studies of high catalytic activity in Au–Pd systems with comparable structure [4,17,31].

In any case, bimetallic catalysts prepared by both routes are more efficient than the corresponding similarly prepared monometallic Au and Pd samples.

The bimetallic [AuPd]/γ-Al_2O_3 and [AuPd]/TiO_2 supported catalysts (route 1) have been reused four batch runs in solvent-free conditions without loss in catalytic activity and selectivity and very low amounts of gold and palladium leached in solution (<0.2% of the total available metal).

The results here reported show an interesting additional example of a strong relation between catalytic properties and structural features in Au–Pd bimetallic catalysts. Moreover, they could suggest the simultaneous vaporization of two metals by metal vapour synthesis technique, a valuable preparative route to bimetallic metal particles which, differently from other preparation ways, can be easily deposited in mild conditions on a wide range of inorganic and organic supports.

Finally, the co-evaporation of Pd and Au metals allows an interaction at the atomic level between Au and Pd vapour as mono- or oligoatomic species in the absence of additional stabilizers, which are often expected in most of other synthetic procedures.

Acknowledgment

This work was partially supported by the Italian Ministry of University and Scientific Research (MIUR) under the PRIN 2008 Program (2008SXASBC_001).

References

[1] N. Toshima, T. Yonezawa, New J. Chem. (1998) 1179. and references therein.
[2] J. Ferrando, J. Jellinek, R.L. Johnston, Chem. Rev. 108 (2008) 845.
[3] L. Guzci, Catal. Today 101 (2005) 53. and references therein.
[4] G.J. Hutchings, Chem. Commun. (2008) 1148.
[5] D.I. Enache, J.K. Edwards, P. Landon, B. Solsona-Espriu, A.F. Carley, A.A. Herzing, M. Watanabe, C.J. Kiely, D.W. Knight, G.J. Hutchings, Science 311 (2007) 362.
[6] D.I. Enache, D. Barker, J.K. Edwards, S.H. Taylor, D.W. Knight, A.F. Carley, G.J. Hutchings, Catal. Today 122 (2007) 407.
[7] A. Villa, C. Campione, L. Prati, Catal. Lett. 115 (2007) 133.
[8] J.K. Edwards, B.E. Solsona, P. Landon, A.F. Carley, A. Herzing, C.J. Kiely, G.J. Hutchings, J. Catal. 236 (2005) 69.
[9] F. Menegazzo, P. Burti, M. Signoretto, M. Manzoli, S. Vankova, F. Boccuzzi, F. Pinna, G. Strukul, J. Catal. 257 (2008) 369.
[10] D. Kumar, M.S. Chen, D.W. Goodman, Catal. Today 123 (2007) 77.
[11] M.S. Chen, D. Kumar, C. Yi, D.W. Goodman, Science 310 (2005) 291.
[12] B. Pawelec, A.M. Venezia, V. La Parola, E. Cano-Serrano, J.M. Campos-Martin, J.L.G. Fierro, Appl. Surf. Sci. 242 (2005) 380.
[13] V.I. Parvulescu, V. Parvulesco, U. Undruschat, G. Filoti, F.E. Wagner, C. Kubel, R. Richards, Chem. Eur. J. 12 (2006) 2343.
[14] M. Bonarowska, A. Malinowski, W. Juszczyk, Z. Kapinski, Appl. Catal. B – Environ. 30 (2001) 187.
[15] H. Okamoto, T.B. Massalki, Bull. Alloy Phase Diagrams 6 (1985) 7.
[16] A.A. Herzing, A.F. Carley, J.K. Edwards, G.J. Hutchings, C.J. Kiely, Chem. Mater. 20 (2008) 1492.
[17] S. Marx, A. Baiker, J. Phys. Chem. C 113 (2009) 6191.
[18] C.H. Chen, L.S. Sarma, J.M. Chen, S.C. Shih, G.R. Wang, G.G. Liu, M.T. Tang, J.F. Lee, B.J. Hwang, ACS Nano 1 (2007) 114.
[19] M. Harada, K. Asakura, N. Toshima, J. Phys. Chem. 97 (1993) 5103.
[20] D. Wang, A. Villa, F. Porta, L. Prati, D.S. Su, J. Phys. Chem. C 112 (2008) 8617.
[21] Y. Ding, F. Fan, Z. Tian, Z. Lin Wang, J. Am. Chem. Soc. 132 (2010) 12480.
[22] A. Beck, A. Horvath, Z. Schay, G. Stefler, Z. Koppany, I. Sajo, O. Geszti, L. Guczi, Top. Catal. 44 (2007) 115.
[23] S. Devarajan, P. Bera, S. Sampath, J. Colloid Interf. Sci. 290 (2005) 117.
[24] G. Vitulli, C. Evangelisti, A.M. Caporusso, P. Pertici, N. Panziera, S. Bertozzi, P. Salvadori, in: B. Corain, G. Schmid, N. Toshima (Eds.), Metal Nanoclusters in Catalysis and Materials Science. The Issue of Size-Control, Elsevier, Amsterdam, 2008 (Chapter 32).
[25] R.A. Sheldon, J.K. Kochi, Metal-Catalyzed Oxidations of Organic Compounds, Academic Press, New York, 1981.
[26] U.R. Pillai, E. Sable-Demessie, Appl. Catal. A: Gen. 245 (2003) 103.
[27] K. Mori, T. Hara, T. Mizugaki, K. Ebitani, K. Kaneda, J. Am. Chem. Soc. 26 (2004) 10657.
[28] A. Abad, P. Conception, A. Corma, H. Garcia, Angew. Chem. Int. Ed. 44 (2005) 4066.
[29] F.M. Menger, C. Lee, Tetrshedron Lett. 22 (1981) 1655.
[30] D.G. Lee, U.A. Spitzer, J. Org. Chem. 35 (1970) 3589.
[31] N. Dimitratos, A. Villa, D. Wang, F. Porta, D. Su, L. Prati, J. Catal. 244 (2006) 113.
[32] J.S. Bradley, in: G. Schmid (Ed.), Clusters and Colloids. From Theory to Applications, VCH, Weinheim, 1994, p. 459.
[33] S. Pascarelli, F. D'Acapito, G. Antonioli, A. Balerna, F. Boscherini, R. Cimino, G. Dalba, P. Fornasini, G. Licheri, C. Meneghini, F. Rocca, S. Mobilio, ESRF Newslett. 23 (1995) 17.
[34] S. Pascarelli, F. Boscherini, F. D'Acapito, J. Hrdy, C. Meneghini, S. Mobilio, J. Synch. Rad. 3 (1996) 147.
[35] P.A. Lee, P.H. Citrin, P. Eisenberger, B.M. Kincaid, Rev. Mod. Phys. 53 (1981) 769.
[36] G. Ciatto, F. d'Acapito, F. Boscherini, S. Mobilio, J. Synch. Rad. 11 (2004) 278.
[37] C. Evangelisti, P. Raffa, G. Uccello-Barretta, G. Vitulli, L. Bertinetti, G. Martra, J. Nanosci. Nanotechnol. 11 (2011) 2226–2231.
[38] L. Marchese, S. Bordiga, S. Coluccia, G. Martra, A. Zecchina, J. Chem. Soc. Faraday Trans. 89 (1993) 3483–3489.
[39] T. Comaschi, A. Balerna, S. Mobilio, Phys. Rev. B 77 (2008) 075432.
[40] J.J. Rehr, R.C. Albers, Rev. Mod. Phys. 72 (2000) 621.
[41] A.L. Ankudinov, B. Ravel, J.J. Rehr, S.D. Conradson, Phys. Rev. B 58 (1998) 7565.
[42] M. Newville, B. Ravel, J. Rehr, E. Stern, Y. Yacoby, Physica B 208–209 (1995) 154.
[43] G.G. Li, F. Bridges, C.H. Booth, Phys. Rev. B 52 (1995) 6332.
[44] T. Comaschi, A. Balerna, S. Mobilio, J. Phys.: Condens. Matter 21 (2009) 325404.
[45] A. Balerna, L. Liotta, A. Longo, A. Martorana, C. Meneghini, S. Mobilio, G. Pipitone, Eur. Phys. J. D 7 (1999) 89.
[46] L.A. Aronica, E. Schiavi, C. Evangelisti, A.M. Caporusso, P. Salvadori, G. Vitulli, L. Bertinetti, G. Martra, J. Catal. 266 (2) (2009) 250.
[47] A. Balerna, E. Bernieri, P. Picozzi, A. Reale, S. Santucci, E. Burattini, S. Mobilio, Phys. Rev. B 31 (1985) 5058.
[48] H.B. Liu, U. Pal, A. Medina, C. Maldonado, J.A. Ascencio, Phys. Rev. B 71 (2005) 075403.
[49] F. Liu, D. Wechsler, P. Zhang, Chem. Phys. Lett. 461 (2008) 254.
[50] C.-M. Lin, T.-L. Hung, Y.-H. Huang, K.-T. Wu, M.-T. Tang, C.-H. Lee, C.T. Chen, Y.Y. Chen, Phys. Rev. B 75 (2007) 125426.
[51] G. Li, D.I. Enache, J. Edwards, A.F. Carley, D.W. Knight, G.J. Hutchings, Catal. Lett. 110 (2006) 7–13.